Coregistration of Ultrasound and Magnetic Resonance Imaging with a Preliminary Investigation of the Spatial Colocalization of VEGFR2 Expression and Tumor Perfusion in a Murine Tumor Model

Mary E. Loveless, MS[1,2,*], **Jennifer G. Whisenant, ME**[1,3,*], **Kevin Wilson, ME**[1], **Andrej Lyshchik, MD, PhD**[4], **Tuhin K. Sinha, PhD**[1,4], **John C. Gore, PhD**[1,2,3,4,5,6], and **Thomas E. Yankeelov, PhD**[1,2,3,4,5,7]

[1]Institute of Imaging Science, Vanderbilt University, Nashville, Tennessee 37232-2675

[2]Department of Biomedical Engineering, Vanderbilt University, Nashville, Tennessee 37232-2675

[3]Department of Chemical & Physical Biology, Vanderbilt University, Nashville, Tennessee 37232-2675

[4]Department of Radiology and Radiological Sciences, Vanderbilt University, Nashville, Tennessee 37232-2675

[5]Department of Physics and Astronomy, Vanderbilt University, Nashville, Tennessee 37232-2675

[6]Department of Molecular Physiology and Biophysics, Vanderbilt University, Nashville, Tennessee 37232-2675

[7]Department of Cancer Biology Vanderbilt University, Nashville, Tennessee 37232-2675

Abstract

We present an US-MRI coregistration technique and examine its application in a preliminary multi-modal, multi-parametric study in a pre-clinical model of breast cancer. Nine mice were injected with 67NR breast cancer cells and imaged 6 and 9 days later with 4.7T MRI and high frequency US. Tumor volumes from each data set were segmented independently by two investigators and co-registered using an iterative closest point algorithm. In addition to anatomical images, VEGFR2 distribution images from the central tumor slice using VEGFR2-targeted UCA and measurements of perfusion and extravascular-extracellular volume fraction using DCE-MRI were acquired from five mice for multi-parametric coregistration. Parametric maps from each modality were co-registered and examined for spatial correlation. Average registration RMS error was 0.36 mm +/- 0.11 mm, less than approximately two voxels. Segmented volumes were compared between investigators to minimize inter-observer variability; average RMS error was 0.23 mm +/- 0.09 mm. In the preliminary study, VEGFR2-targeted UCA data did not demonstrate direct spatial correlation with MR measures of vascular properties. In summary, a method for accurately co-registering small animal US and MRI has been presented which allows for comparison of quantitative metrics provided by the two modalities.

Please address correspondence to: Thomas E. Yankeelov, PhD Institute of Imaging Science Vanderbilt University Medical Center 1161 21st Ave. South, MCN AA-1105 Nashville, TN 37232-2675 USA Tel: (615) 322-8354 Fax: (615) 322-0734 Email: thomas.yankeelov@vanderbilt.edu.
*Authors contributed equally to this work

Introduction

In order for a tumor to grow beyond approximately 1-2 mm^3, it must recruit and form new vasculature as it can no longer rely on the passive diffusion of nutrients [1]. During this process of angiogenesis several growth factors, including vascular endothelial growth factor (VEGF), are released from both tumor and endothelial cells, and new vessels develop in response to these [2]. With the development of vascular-specific contrast agents, medical imaging techniques have become much more sensitive to particular aspects of angiogenesis [3,4]. For example, the advent of contrast enhanced ultrasound (CEUS) using microbubbles targeted to specific receptors permits the study of angiogenesis at a molecular level [5,6]. A specific target that has been studied using CEUS is VEGF receptor 2 (VEGFR2), a well characterized pro-angiogenic receptor for VEGF type A [7]. In addition, it has been shown that dynamic contrast enhanced magnetic resonance imaging (DCE-MRI) can assess physiological characteristics such as perfusion, blood vessel permeability, extravascular extracellular volume fraction, and blood volume [8,9]. These parameters are extracted from models fit to time-intensity curves that describe the kinetics of an injected contrast agent as it enters and exits a region of interest. Combining these two modalities could provide complementary information about tumor vasculature by fusing both physiological (DCE-MRI) and molecular (targeted CEUS) data. Moreover, correlations and comparisons of these types of data may be useful for their proper interpretation; both measures have been used independently as a measure of treatment response [6,9]. Combining these metrics could provide more information about the status of the tumor that may predict treatment response faster than using the two measures independently.

The ability to accurately co-register imaging data obtained from different modalities can in principle provide a more complete characterization of tumor status in clinical applications, as well as new insights into tumor biology and drug testing in pre-clinical studies. One motivation for multi-modality imaging is that any technique has its own set of strengths and weaknesses, and appropriate combinations of modalities can not only increase existing strengths but also alleviate existing weaknesses. A primary example of this is PET-CT (positron emission tomography and X-ray computed tomography, respectively) whereby the molecular data provided by PET is registered with high resolution structural imaging from CT to provide anatomical landmarks for areas of increased tracer activity. Indeed, the combination of structural and functional imaging data is well known and has been covered in several excellent reviews [10,11]. More recently, efforts have been made to combine imaging modalities in order to evaluate cancer across biological scales; for example, MRI and PET have been co-registered to investigate the relationship between hypoxia measured by fluorine-18 fluoromisonidazole (^{18}FMISO)-PET and perfusion measured with DCE-MRI [12]. However, two modalities that have not previously been intimately combined for multi-parametric studies of pre-clinical models of cancer are ultrasound (US) and MRI.

In this study we present an approach that facilitates the Coregistration of small animal US and MR imaging data of a subcutaneous, pre-clinical tumor model; to the best of our knowledge, this is the first such study. While there have been excellent contributions on the registration of human US and MRI data [13,14], there is a paucity of data in the small animal setting which has its own set of obstacles. Additionally, we provide a relevant example of an application with this technique by examining the relationship between the molecular information derived using a VEGFR2-targeted ultrasound contrast agent (UCA)

and physiological information about tumor perfusion and vascular permeability using DCE-MRI. The results of this study suggest that the relationship between physiological and molecular biomarkers of angiogenesis is indeed more complex than our initial hypothesis of direct spatial correlation.

Materials and Methods

Tumor Model

Murine 67NR breast cancer cells have been shown to express increased levels of VEGFR2 as measured by targeted CEUS [5,15]. These cells were cultured in Dulbecco's modified Eagle's medium supplemented with 10% fetal bovine serum and 0.2% Gentamicin. Cells were incubated at 37° C in a mixture of 5% carbon dioxide and 95% air. Cells growing at 80% confluence were harvested, and a single cell suspension containing 5×10^6 cells suspended in 100-μL of medium was injected subcutaneously near the flank. Tumors were allowed to grow for 6 to 9 days before imaging.

Animal Model

Nine adult female nu/nu mice (18-20 g, 8-10 weeks of age) were purchased from Charles River Laboratories (Wilmington, MA), housed in pathogen-free facilities with a 12-hour light/dark cycle (6 AM-6 PM), and provided with rodent chow and tap water *ad libitum*. For targeted CEUS /DCE-MRI studies, a 26-gauge jugular catheter was surgically implanted to allow for delivery of US and MRI contrast agents. All animals were imaged at two time points; the second time point occurred 48 hours after the first imaging session. All animal procedures were approved by and adhered to our Institutional Animal Care and Use Committee guidelines.

Ultrasound Contrast Agent Preparation

MicroMarker Target-Ready (Visualsonics, Inc, Toronto, Ontario, Canada) contrast agent was prepared and used according to manufacturer guidelines. This agent consists of microbubbles (2-3 μm in diameter) with a lipid-based shell that has streptavidin incorporated to allow maximum binding of biotinylated target antibodies. Approximately 9.2×10^8 dry microbubbles were reconstituted using 500 μL of sterile saline. Then, 20 μg of biotinylated antimouse VEGFR2 antibodies (eBioscience Inc, San Diego, CA) were diluted to a total volume of 400 μL and added to the vial of reconstituted microbubbles, as per manufacturer's instructions. The vial containing both the VEGFR2 antibodies and microbubbles were gently agitated for one minute and allowed to bind for 15 minutes.

Data Acquisition

Magnetic Resonance Imaging—The mice were anesthetized using a 2%/98% isoflurane/oxygen mixture and placed in a custom built mouse restraint to keep the animals stationary for transport between modalities. Body temperature was maintained *via* a flow of warm air through the magnet bore or warming plate on the US imaging stage. Temperature and respiratory rate were monitored throughout the entire experiment.

Figure 1 displays the imaging protocols used in the study. MR imaging employed a Varian 4.7 T Inova scanner (Varian, Inc. Palo Alto, CA) equipped with a 38-mm quadrature coil. After the tumor region was localized *via* low-resolution spin echo sequences, three data sets were acquired: 1) high-resolution anatomical images covering the entire tumor for the purpose of co-registration with US; 2) a pre-contrast T_1 map as required for quantitative DCE-MRI analysis; and, 3) DCE-MRI data for the purpose of correlating with US characterization of VEGFR2 expression (see below). For the high resolution data set on

tumors smaller than approximately 100 mm^3, a spin echo pulse sequence with a repetition time (*TR*) of 4500 ms and an echo time (*TE*) of 30 ms was used to acquire 128^2 T_2-weighted axial images over a 35 mm^2 field of view (FOV). The slice thickness was 0.25 mm, yielding a voxel size of 0.018 mm^3. The number of excitations (NEX) was 8. For tumors larger than 100 mm^3, the following parameters were used: *TR\TE* = 3000 ms\ 30 ms, slice thickness = 0.3 mm, and NEX = 6 to acquire $128^2 T_2$ weighted axial images over a 35^2 mm FOV (voxel size ≈ 224 μm^3).

For both the T_1 mapping and DCE-MRI acquisitions, the central ten 1.0 mm thick slices of the tumor were selected for imaging. Data for constructing a pre-contrast T_1 map were obtained by employing a variable flip angle gradient echo sequence with flip angles of 8°, 16°, 24°, 32°, and 40°. Imaging parameters were *TR\TE* = 200 ms\ 2.83 ms and NEX = 4, FOV = 35 mm^2, matrix = 128^2. The DCE-MRI protocol employed a T_1-weighted, gradient echo sequence to obtain 70 serial images for each set of ten axial planes, translating to a temporal resolution of 25.6 seconds for each image set acquisition for 40 minutes. The parameters were: *TR\TE*α = 100 ms\2.83 ms\25°, NEX = 2, with the same acquisition matrix and FOV as for the T_1 map. A bolus of 0.2 mmol/kg gadopentetate dimeglumine (Magnevist, Wayne, NJ) was delivered over 20 seconds *via* a jugular catheter beginning after the acquisition of the fifth dynamic image.

Ultrasound Imaging—After MRI, anesthesia was maintained as above, and the animal was transferred to a Visualsonics Vevo 770 high frequency ultrasound imaging system (Visualsonics Inc, Toronto, Ontario, Canada) equipped with a 40-MHz center-frequency transducer with a mechanically scanned, single-element aperture. Coupling gel was applied to cover the entire region of interest, and 2-D B-mode scout images established the central slice of the tumor. The transducer was placed such that the 6 mm focal spot converged at the center of the tumor. After tumor localization, two data sets were acquired: 1) 3-D anatomical B-mode images covering the entire tumor for the purpose of coregistration with MRI; and, 2) images from the central slice of the tumor showing VEGFR2 distribution as estimated by targeted microbubbles. Anatomical B-mode images at 100% power (mechanical index (M.I.) of 0.50) were acquired using a 512^2 acquisition matrix and a 10 to 15-mm^2 FOV (depending on the size of the tumor). The transducer was automatically incremented by a 3-D motor with a 0.102 mm step size over the entire tumor volume, yielding an effective voxel size of 36 to 84 μm^3.

The VEGFR2-targeted UCA protocol in this study was followed per manufacture recommendation. A bolus of approximately 5.1×10^7 targeted microbubbles in 50 μL of saline was injected *via* jugular catheter, followed by a 10 μL saline flush. Images were acquired in Contrast Mode at 50% power (M.I. of 0.14). Following the protocol illustrated in Figure 1, imaging was halted four minutes to allow optimal binding of the targeted UCA. Image acquisition resumed acquiring 150-200 frames at a frame rate of 14 frames/second followed by a high powered destruction sequence (20 cycles at a frequency of 10 MHz and an M.I. = 0.59). After this sequence, imaging parameters were returned to the previously set parameters and 200 reference images were acquired.

Data Analysis

Magnetic Resonance Imaging—High-resolution anatomical MR data were exported to Matlab R2007a (The Mathworks, Natick, MA, USA) for segmentation and registration. DCE-MRI data analysis was performed using routines written in IDL (Research Systems, Inc, Boulder, CO). The T_{10} maps (i.e., a map of T_1 values before contrast was administered) were obtained by fitting the variable flip angle spoiled gradient echo data to Eq. 1:

$$S = S_0 \cdot \left[\sin(\alpha) \cdot (1 - exp(-TR/T_{10})) / (1 - (exp(-TR/T_{10}) \cdot \cos(\alpha))) \right],$$

(1)

where α is the flip angle, S_0 is a constant that includes scanner gain and proton measurements, and $TE \ll T_2^*$ is assumed. These T_{10} maps were used to estimate relaxation rate $R_1 (\equiv 1/T_1)$ time courses for each voxel in the tissue of interest (TOI). Maps of K^{trans} (the blood perfusion-vessel permeability product) and v_e (extravascular-extracellular volume fraction) were created using a reference region (RR) method outlined in detail in reference [16]. Briefly, the reference region (RR) calibrates signal intensity changes in the regions of interest (e.g., a tumor) to that in a well-characterized reference region (e.g., muscle). The end result of the theory is a practical equation which does not require the measurement of an arterial input function (i.e., the time rate of change of contrast agent in the blood pool). It is important to note that a significant advantage of reference region modeling is that it does not require high temporal resolution data to quantitatively analyze the R_1 time courses [14]. The theory (in the fast exchange limit [17]) is summarized by Eq. 2:

$$R_1^{TOI}(T) = R \cdot \left(R_1^{RR}(T) - R_{10}^{RR} \right) + R \cdot \left[\left(K^{trans,RR}/V_{e,RR} \right) - \left(K^{trans,TOI}/V_{e,TOI} \right) \right]$$
$$\cdot \int_0^T \left(R_1^{RR}(t) - R_{10}^{RR} \right) \cdot exp\left(-K^{trans,TOI}/V_{e,TOI} \right) \cdot (T - t)) \, dt + R_{10}^{TOI},$$

(2)

where R_1^{RR} and R_1^{TOI} are the longitudinal relaxation rate constants in the RR and TOI, respectively; $K^{trans,RR}$ and $K^{trans,TOI}$ are the contrast agent extravasation rate constants for the RR and TOI, respectively; $v_{e,RR}$ and $v_{e,TOI}$ are the extravascular extracellular volume fractions for the RR and TOI, respectively; R_{10} is the pre-contrast R_1; and $R = K^{trans,TOI}/K^{trans,RR}$. Equation 2 has four free parameters: $K^{trans,TOI}$, $K^{trans,RR}$, $v_{e,TOI}$, and $v_{e,RR}$. We fix $v_{e,RR}$ at the reasonable value of 0.08 [18, 19] and employ a two-step process to estimate $K^{trans,RR}$ before proceeding to a voxelby-voxel analysis to obtain $K^{trans,TOI}$ and $v_{e,TOI}$ parametric maps. Details are provided elsewhere [19]. Briefly, for each mouse, 25 voxels within the perivertebral muscle were selected as the RR and 75 voxels within the tumor were selected as a large, high signal-to-noise TOI. A three parameter fit ($K^{trans,TOI}$, $K^{trans,RR}$, and $v_{e,TOI}$) was performed to obtain an estimate of $K^{trans,RR}$. This process was repeated five times from which a mean $K^{trans,RR}$ was obtained. $K^{trans,RR}$ in Equation 2 was then fixed at this value so that a subsequent two-parameter ($K^{trans,TOI}$ and $v_{e,TOI}$) analysis could be performed on all individual voxels within the tumor for each of the 10 slices created. The resulting $K^{trans,TOI}$ and $v_{e,TOI}$ parametric maps were aligned to the anatomical MRI data by determining the offsets from the high resolution anatomical data set within the bore of the magnet. These maps were imported to Matlab for coregistration and correlation analysis.

Ultrasound—High-resolution 3-D anatomical B-mode US image sets were exported to Matlab R2007a for segmentation and registration. For computational ease, US data sets were downsampled from an acquisition matrix of 512^2 to 256^2. Image processing for the VEGFR2 US data was performed using the Vevo 770 software. All image data, including reference and data frames, were log compressed, digitized to 12 bits, and then further compressed to 8 bits for screen display. Reference images were gathered immediately after the destruction sequence. Each pre-destruction frame was compared with each reference frame by an absolute sum-of-differences method to allow for the pairing of two images with the smallest total difference for subtraction:

$$\Delta[i] = \sum_{i=1}^{n} (reference \quad image \quad [i] - data \quad image \quad [i])^2,$$

(3)

where the reference image is a post-destruction frame and the data image is a pre-destruction frame. Once these images were paired, a subtracted image was generated which presents an estimate of only the bound VEGFR2 microbubbles (pre-destruction frame containing both bound and unbound CA - post-destruction frame containing unbound,freely-circulating CA) within the FOV. This processed image was then exported to Matlab R2007a for registration to the MRI data and subsequent correlation analysis.

Segmentation and Registration—Two investigators manually segmented tumor volumes from each MRI and US data set independently. Each corresponding segmented surface from MRI and US was manually aligned and then registered to one another using an iterative closest point (ICP) algorithm [20]. This algorithm registers two 3-D shapes by discretizing each surface into a set of points, and rigidly aligning one to the other in an iterative fashion. At each iteration, a transformation is found by calculating closest point pairs between each shape and finding an optimal translation and rotation to minimize the root mean square (RMS) distance between all point pairs. This transform is applied to the one dataset before the next iteration begins (104 maximum iterations were allowed). The registration is complete when the solution reaches convergence within a predefined threshold. Our application of the ICP algorithm followed the manual registration so that the surfaces were already well-aligned, thus limiting the potential for inappropriate convergence of the algorithm. A custom animal holder was built so that the animal was not allowed to move between the US and MRI examinations. This limited the change in position and orientation of the tumor relative to the surrounding tissue and allowed us to use rigid alignment techniques to provide accurate coregistration between the two modalities. Also, it is well-known that ICP approaches have limitations when registering objects with high degrees of symmetry [20], We were concerned that the tumor surfaces acquired via US and MRI would not provide the required geometric anisotropy for accurate ICP refinement. However, in our experience, the tumor surfaces in each modality contained enough geometric features such that the ICP alignment did not converge to obviously incorrect solutions. Rather, the ICP approach correctly registers the manual registration in all cases studied. When coupled in this fashion, the manual coregistration and automatic refinement provided sufficiently accurate coregistrations for our voxel-by-voxel correlation analysis. As a measure of coregistration accuracy, RMS errors between the surfaces defined for each modality were recorded for each registration and compared between investigators. RMS errors were also compared between segmented data sets from each investigator to assure minimum error contribution from segmentation.

Correlation Analysis—Anatomical B-mode US and 2-D multi-slice T_2-weighted anatomical images were segmented and registered to US space using the ICP algorithm described above. Once the MRI to US transformation was found, it was applied to the maps of K^{trans} and v_e. Slices containing intensities from the VEGFR2 bound UCA, K^{trans}, and v_e were then analyzed using the Pearson correlation coefficient determined by the Matlab command `corrcoef' on a voxel-by-voxel basis within the tumor region.

Results

The coregistration steps employed for this study are displayed in Figure 2. The entire tumor volume was manually outlined from each MRI and US image slices (Figures 2A and 2D). Segmented US data were registered to MRI segmentation data (Figures 2B and 2E), and contour lines (blue and green) and cross hairs (yellow) were drawn to show the voxel-to-voxel registration. Figure 2F depicts one slice from the registered and segmented US data, where the signal intensity is represented with a different colormap so that overlaid MRI-US images are easier to visualize.

Additional registration results for two mice at each time point are shown in Figure 3. Panels A-D represent one mouse at both time points while panels E-H display the registration of another subject at both time points.

RMS errors for this study are listed in Table 1. Average RMS error for all time points was 0.36 mm with a standard deviation of 0.11 mm, which is approximately less than two voxels. Before segmentation, both investigators agreed on location of general tumor characteristics, such as tumor tissue, subcutaneous fat, and hyper-echogeneity of the skin, to more accurately define tumor boundaries. Each investigator then performed segmentation independently.

The use of two independent users allowed for investigation of segmentation variability for each modality and the effect on registration error. Volumes were calculated for all segmentations. The average volume (`·`) was determined and errors for each modality (where a vertical indicates the error in US volume, and a horizontal line indicates the error for MRI volume) are shown in Figure 4A; the error was defined as the distribution of segmented tumor volumes from both investigators. The line of unity (solid line) demonstrates the accuracy of the segmentation volumes between investigators ($y = 0.98x + 1.84$, $r = \sim 1.00$, $p < 0.05$). The average RMS error for the segmentation comparison was 0.23 mm +/- 0.09 mm. Values for each subject are listed in Table 2.

As the tumor increased in volume over time, a slight increase in RMS error was noted and is displayed in Figure 4B ($y = 7.0 \times 10^{-4}x + 0.25$, $r = 0.66$, $p < 0.05$). To understand this trend further, error in segmentation between investigators was examined across the increasing volumes shown in Figure 5A. Since segmentation error also increased ($y = 5.0 \times 10^{-4}x + 0.15$, $r = 0.68$, $p < 0.05$), segmentation error was graphed as a function of modality, and from Figure 5B, larger and more variable error was found with the US segmentation.

Five of the mice examined in the registration study were used to perform preliminary investigations regarding the relationship between VEGFR2 as reported with targeted CEUS and perfusion measurements obtained from DCE-MRI. Pearson correlation coefficients were computed for each of the five mice at two different time points with the exception of mouse 7 that, due to problems with the jugular catheter, only provided data from the first time point. Additionally, an error occurred during injection for mouse 9 at time point 2, and no usable data were acquired. Figure 6 demonstrates the step-by-step method for registering the DCE-MRI maps to US space.

After segmentation (panels A and D), MRI data were registered to US, shown in Figure 6B and 6E. The transformation was then applied to the maps for each modality with the results shown in panels C and F. The voxel-by-voxel correlation analysis investigating the relationships between VEGFR2 and both K^{trans} and v_e within the tumor region yielded no significant spatial correlation. These preliminary results seem to indicate no direct spatial relationship between the distribution of VEGFR2 as estimated by CEUS and the pharmacokinetic parameters afforded by DCE-MRI (r = -0.06, p < 0.05). Figure 7 confirms this visually by presenting 2 additional mice at two time points with corresponding VEGFR2 distribution maps (panels A, D, G, J), K^{trans} (panels B, E, H, K) and v_e (panels C, F, J, L) on the central slice of the tumor.

While we did not expect to find a direct spatial correlation between VEGFR2 expression and v_e, a direct correlation between measurements of VEGFR2 and the volume rate transfer constant K^{trans} was anticipated. In order to investigate the nature of this relationship more fully, a temporal analysis was performed on the mice that had at least two time points. Histograms of identical ROIs in the center and rim of the tumor were examined for each parametric map at each time point. Preliminary findings showed no distinguishable pattern

in fluctuations of VEGFR2 and changes in perfusion (K^{trans}); however, more subjects are needed to obtain a conclusive result. [21]

Discussion

During pre-clinical studies of anti-cancer drugs and/or treatment efficacies, multiple imaging modalities are often employed to report on the physiological and/or molecular changes that occur [22,23]. Tumors are well-known to exhibit a variable phenotype, so obtaining multiple measurements from the same animal during a study is potentially advantageous to provide a more comprehensive understanding of tumor-host-drug interaction. In addition to combining various metrics on the same animal, multi-modal coregistration permits corroboration of similar metrics obtained by different imaging techniques. The coregistration method presented in this study demonstrates, for the first time, the capability of combining small animal MRI and US data to examine the relationship of two potential biomarkers of angiogenesis in a pre-clinical cancer model.

Due to the non-rigid, complex, and variable anatomy of tumors, the ICP algorithm was chosen over landmark-based registration techniques, which require external anatomical fiducials. It was also chosen over intensity-based techniques such as mutual information, because there is insufficient information overlap between the US and MR images in many subcutaneous tumor models (unpublished results). Difficulties arise when registering data based on voxel information due to differences in FOV and modality-specific image contrast and noise [13]. The custom animal holder allowed for the definition of a reliable initial position assignment required for convergence of the ICP algorithm to a true positive result. The ICP registration algorithm returns a transformation that minimizes the distance between corresponding points along the MRI and US surfaces. This distance is averaged and recorded as RMS error for each transformation. This metric provides a measure of how well the US reference shape fits the MRI target. Our registration errors are similar to those obtained in previous studies. For example, other groups have recorded average RMS errors of 7.6 mm (approximately five voxels) for clinical and 0.35 mm (approximately two voxels) for pre-clinical coregistration of CT and MRI [24,25]. Barratt, et al. reported average RMS errors of 3.3 mm (approximately four voxels on clinical equipment) when using an ICP algorithm for coregistration of US and CT of cadaver bones [26].

The ability to visualize tumor margins is an important factor for the accuracy of this registration technique. Therefore, ICP registration errors would increase if the surfaces of interest were no longer distinguishable from the background. Considering Table 2, the average segmentation error for MRI between time points is similar and has low variability. It is well known that MRI has excellent soft tissue contrast and therefore tumor margins (for these subcutaneous tumors studies) were easily visible. It can also be deduced from Figure 5B that the difference in average segmentation error between time points is significant for US. It became increasingly difficult with increasing volume to determine tumor boundaries on the US images because a tradeoff exists between depth of penetration and image resolution. For this study, a 40 MHz US transducer was used because high spatial resolution is desirable for accurate registration and investigation into murine models of cancer. However as the volume increased, the majority of the tumor was no longer in the focal zone of the transducer resulting in difficulties visualizing the lower tumor boundaries at time point two. The use of a transducer with a lower frequency might improve the ability to visualize the lower boundary on larger tumors, but the decreased in-plane spatial resolution might make differentiating between the tumor and surrounding tissue more difficult. In addition to the difficulty with depth penetration, the skin exhibited hyper-echogeneity, or increased signal intensity. Other tissues, including tumor and subcutaneous fat, also exhibited similar characteristics which led to difficulty determining side, upper and lower

tumor boundaries. Investigators agreed upon the differences between skin, fat and tumor tissues; to compensate for ambiguity of tumor boundaries during independent segmentation, investigators attempted to use the whole 3D tumor volume to interpret tumor boundaries, such as in Figure 1. Conversely, though MRI has excellent soft tissue contrast, it cannot acquire images at the same spatial resolution (in reasonable scan times) as US. Typical in-plane and through-plane resolutions for a quantitative image acquisition protocol such as DCE-MRI are approximately 200 μm and 500 μm, respectively (for an approximately one hour scan time); thus, tumors must be large enough for detection using MRI. Each modality has advantages and disadvantages that are important factors to consider when using this registration technique; a proper tumor volume range is essential such that RMS errors are minimized.

Preliminary data were collected during this study to show the possibility of combining metrics from both US and MRI. Based on the results of the VEGFR2 and DCE-MRI parameter comparison, the lack of direct spatial correlation suggests several possible avenues of investigation. The initial hypothesis investigated in this study suggested that VEGFR2 expression and the DCE-MRI parameter reporting on vascular perfusion and permeability (K^{trans}) would positively correlate because both are biomarkers of angiogenic activity in cancer. While only five mice were studied, no spatial correlation was found between these two parameters. In fact, the images shown in Figure 7 indicate (qualitatively) that areas of higher VEGFR2 expression might co-localize with regions of low perfusion and/or permeability. The consistently low correlation values found suggest that these parameters may have a more complex relationship; because these two biomarkers of angiogenesis measure different scales of activity, molecular and physiological, a lack of direct spatial correlation might not be surprising. The true relationship between these measures may be better expressed as a spatiotemporal correlation.

Shalaby, et al showed the importance of VEGFR2 expression for vascular maturation by demonstrating that absence of VEGFR2 resulted in disturbed differentiation of endothelial cells causing embryonic death in mice between days eight and nine [27]. Other studies have probed the role of VEGFR2 in downstream effects of endothelial cell proliferation and migration toward hypoxic tissue [28,29]. The binding of VEGF to VEGFR2 initiates a cascade of events that result in the development of mature vessels. Enzymes are released by endothelial cells that break down the surrounding extracellular matrix. Endothelial cells then migrate and proliferate as a chemotactic response to concentrations of VEGF; finally, they reorganize into tubes to form new mature vessels. Thus, the upregulation of VEGFR2 appears to happen as a precursor to vessel formation, establishing a potential time lag between the molecular VEGFR2 metric and measurements of perfusion. This potential time lag has yet to be well defined. As discussed in work reported by Li, et al in a skin window model, vessels dilate and alter their shape in response to proliferating tumor cells in as early as 1-2 days [30]. Neovasculature can be seen in as little as eight days, post tumor implantation. Thus, while the time line of VEGFR2 expression and the resulting formation of perfused vessels is not definitive, the technique presented in this work offers a mechanism for noninvasively investigating this important relationship.

This effort has shown that US and MRI can be co-registered accurately in pre-clinical subcutaneous tumor models, and preliminary findings to a potential application of this technique have been presented. This US-MRI registration technique offers a way to noninvasively image two different angiogenic biomarkers in the same animal, providing a mechanism for further investigating this complex relationship that might not otherwise be easily characterized with *in vivo* pre-clinical models. In addition, the approach described here can return multiple biomarkers for individual animals in order to better characterize the efficacy of various anti-cancer treatments. Finally, since MRI is readily co-registered to

other common tomographic techniques [31], the registration between US and MRI could be further extended to allow cross validation of probes in other molecular imaging modalities such as PET and single photon emission computed tomography that are coupled with CT images. By this merit, this method has the potential to become a valuable tool for multi-modal studies of small animal cancer models.

Acknowledgments

Abbreviations

CEUS	contrast enhanced ultrasound
CT	X-ray computed tomography
DCE	dynamic contrast enhanced
FOV	field of view
ICP	iterative closest point
MI	mechanical index
MRI	magnetic resonance imaging
NEX	number of excitations
PET	positron emission tomography
RMS	root mean square
RR	reference region
TE	echo time
TOI	tissue of interest
TR	repetition time
UCA	ultrasound contrast agent
US	ultrasound
VEGF	vascular endothelial growth factor
VEGFR2	vascular endothelial growth factor receptor 2

References

[1]. Folkman J. Tumor angiogenesis: therapeutic implications. N Engl J Med. 1971; 285:1182–6. [PubMed: 4938153]

[2]. Folkman J, Klagsbrun M. Angiogenic factors. Science. 1987; 235:442–7. [PubMed: 2432664]

[3]. Hsu AR, Chen X. Advances in anatomic, functional, and molecular imaging of angiogenesis. J Nucl Med. 2008; 49:511–4. [PubMed: 18375921]

[4]. Barrett T, Brechbiel M, Bernardo M, Choyke PL. MRI of tumor angiogenesis. J Magn Reson Imaging. 2007; 26:235–49. [PubMed: 17623889]

[5]. Lyshchik A, Fleischer AC, Huamani J, et al. Molecular imaging of vascular endothelial growth factor receptor 2 expression using targeted contrast-enhanced high-frequency ultrasonography. J Ultrasound Med. 2007; 26:1575–86. [PubMed: 17957052]

[6]. Willmann JK, Paulmurugan R, Chen K, et al. US imaging of tumor angiogenesis with microbubbles targeted to vascular endothelial growth factor receptor type 2 in mice. Radiology. 2008; 246:508–18. [PubMed: 18180339]

[7]. Kerbel R, Folkman J. Clinical translation of angiogenesis inhibitors. Nat Rev Cancer. 2002; 2:727–39. [PubMed: 12360276]

[8]. Tofts PS, Brix G, Buckley DL, et al. Estimating kinetic parameters from dynamic contrast-enhanced T(1)-weighted MRI of a diffusable tracer: standardized quantities and symbols. J Magn Reson Imaging. 1999; 10:223–32. [PubMed: 10508281]

[9]. Yankeelov TE, Gore JC. Contrast enhanced magnetic resonance imaging in oncology: data acquisition, analysis, and examples. Current Medical Imaging Reviews. 2007; 3:91–107. [PubMed: 19829742]

[10]. Townsend DW. Multimodality imaging of structure and function. Phys Med Biol. 2008; 53:R1–R39. [PubMed: 18263942]

[11]. Weber DA, Ivanovic M. Correlative image registration. Semin Nucl Med. 1994; 24:311–23. [PubMed: 7817202]

[12]. Zanzonico PB. Broad-spectrum multi-modality image registration: from PET, CT, and MRI to autoradiography, microscopy, and beyond. Conf Proc IEEE Eng Med Biol Soc. 2006; 1:1584–8. [PubMed: 17946908]

[13]. Slomka PJ, Mandel J, Downey D, Fenster A. Evaluation of voxel-based registration of 3-D power Doppler ultrasound and 3-D magnetic resonance angiographic images of carotid arteries. Ultrasound Med Biol. 2001; 27:945–55. [PubMed: 11476929]

[14]. Roche A, Pennec X, Malandain G, Ayache N. Rigid registration of 3-D ultrasound with MR images: A new approach combining intensity and gradient information. IEEE Transactions On Medical Imaging. 2001; 20(10):1038–1049. [PubMed: 11686439]

[15]. Aslakson CJ, Miller FR. Selective events in the metastatic process defined by analysis of the sequential dissemination of subpopulations of a mouse mammary tumor. Cancer Res. 1992; 52:1399–405. [PubMed: 1540948]

[16]. Yankeelov TE, Luci JJ, Lepage M, et al. Quantitative pharmacokinetic analysis of DCE-MRI data without an arterial input function: a reference region model. Magn Reson Imaging. 2005; 23:519–29. [PubMed: 15919597]

[17]. Landis CS, Li X, Telang FW, et al. Equilibrium transcytolemmal water-exchange kinetics in skeletal muscle in vivo. Magn Reson Med. 1999; 42:467–78. [PubMed: 10467291]

[18]. Padhani AR, Hayes C, Landau S, Leach MO. Reproducibility of quantitative dynamic MRI of normal human tissues. NMR Biomed. 2002; 15:143–53. [PubMed: 11870910]

[19]. Yankeelov TE, Cron GO, Addison CL, et al. Comparison of a reference region model with direct measurement of an AIF in the analysis of DCE-MRI data. Magn Reson Med. 2007; 57:353–61. [PubMed: 17260371]

[20]. Besl PJ, McKay HD. A method for registration of 3-D shapes. IEEE Trans Pattern Anal Machine Intell. 1992; 14:239–56.

[21]. Lee Z, Sodee DB, Resnick M, Maclennan GT. Multimodal and three-dimensional imaging of prostate cancer. Comput Med Imaging Graph. 2005; 29:477–86. [PubMed: 15893911]

[22]. Hsu AR, Cai W, Veeravagu A, et al. Multimodality molecular imaging of glioblastoma growth inhibition with vasculature-targeting fusion toxin VEGF121/rGel. J Nucl Med. 2007; 48:445–54. [PubMed: 17332623]

[23]. Babsky AM, Zhang H, Hekmatyar SK, et al. Monitoring chemotherapeutic response in RIF-1 tumors by single-quantum and triple-quantum-filtered (23)Na MRI, (1)H diffusion-weighted MRI and PET imaging. Magn Reson Imaging. 2007; 25:1015–23. [PubMed: 17707164]

[24]. Somer EJ, Benatar NA, O'Doherty MJ, et al. Use of the CT component of PET-CT to improve PET-MR registration: demonstration in soft-tissue sarcoma. Phys Med Biol. 2007; 52:6991–7006. [PubMed: 18029989]

[25]. Batiste DL, Kirkley A, Laverty S, et al. High-resolution MRI and micro-CT in an ex vivo rabbit anterior cruciate ligament transection model of osteoarthritis. Osteoarthritis Cartilage. 2004; 12:614–26. [PubMed: 15262241]

[26]. Barratt DC, Chan CS, Edwards PJ, et al. Instantiation and registration of statistical shape models of the femur and pelvis using 3D ultrasound imaging. Med Image Anal. 2008; 12:358–74. [PubMed: 18313973]

[27]. Shalaby F, Rossant J, Yamaguchi TP, et al. Failure of blood-island formation and vasculogenesis in Flk-1-deficient mice. Nature. 1995; 376:62–6. [PubMed: 7596435]

[28]. Morales-Ruiz M, Fulton D, Sowa G, et al. Vascular endothelial growth factor-stimulated actin reorganization and migration of endothelial cells is regulated via the serine/threonine kinase Akt. Circ Res. 2000; 86:892–6. [PubMed: 10785512]

[29]. Mazure NM, Chen EY, Laderoute KR, Giaccia AJ. Induction of vascular endothelial growth factor by hypoxia is modulated by a phosphatidylinositol 3-kinase/Akt signaling pathway in Ha-ras-transformed cells through a hypoxia inducible factor-1 transcriptional element. Blood. 1997; 90:3322–31. [PubMed: 9345014]

[30]. Li CY, Shan S, Huang Q, et al. Initial stages of tumor cell-induced angiogenesis: evaluation via skin window chambers in rodent models. J Natl Cancer Inst. 2000; 92:143–7. [PubMed: 10639516]

[31]. Judenhofer MS, Wehrl HF, Newport DF, et al. Simultaneous PET-MRI: a new approach for functional and morphological imaging. Nat Med. 2008; 14:459–65. [PubMed: 18376410]
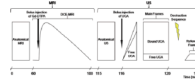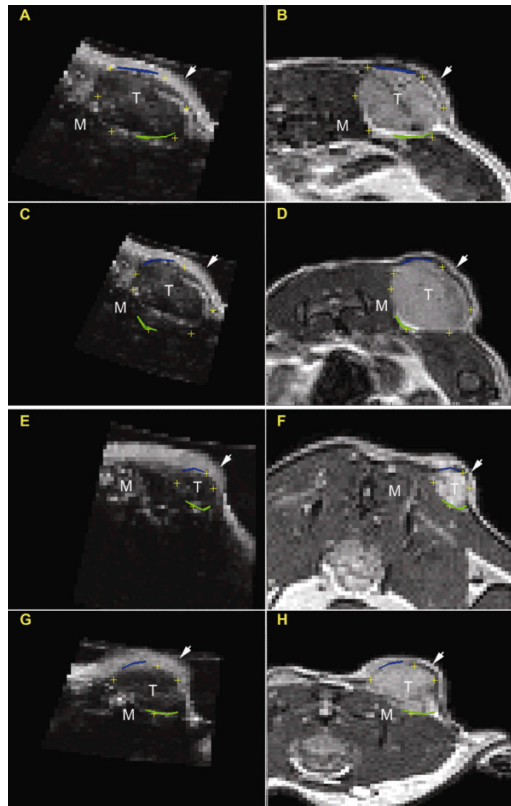
Figure 1.
Time line of the imaging protocols used in this study. A minimum of ~1.5 hours are required for high resolution anatomical and DCE-MRI data acquisition. The VEGFR2-targeted UCA requires four minutes, per manufacturer's guidelines, to bind *in vivo*. A destruction pulse is administered, destroying all UCA so that the unbound contrast agent that flow into the region (Reference frames) can be subtract from the frames containing both
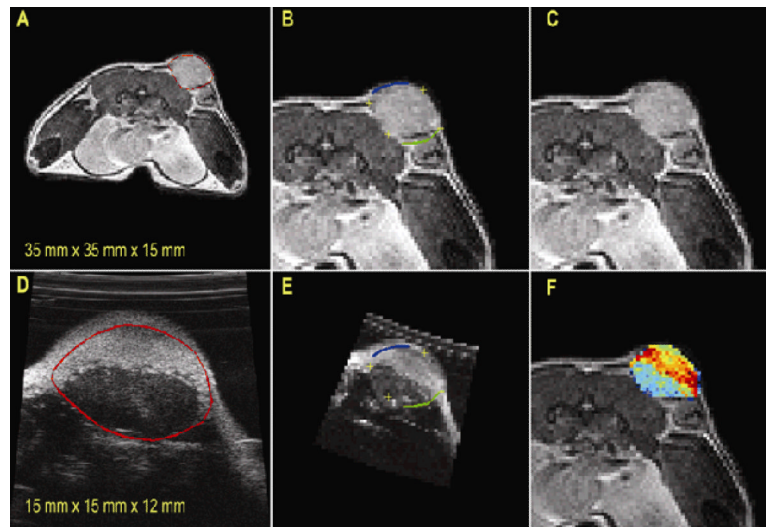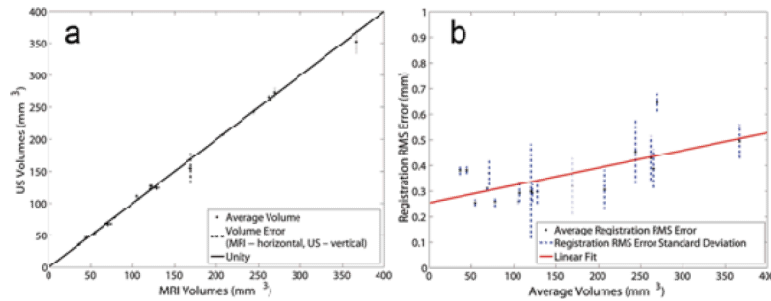
Figure 2.
US and MRI coregistration steps. Tumor margins were manually segmented from MRI and US images (A,D); contour lines (blue and green) and cross hairs (yellow) were drawn to demonstrate registration results (B,E); for clarity, segmented tumor volume from US ("jet" color scheme) was overlaid on MRI (C,F). Note the difference in FOV listed at the bottom of panels a and d.
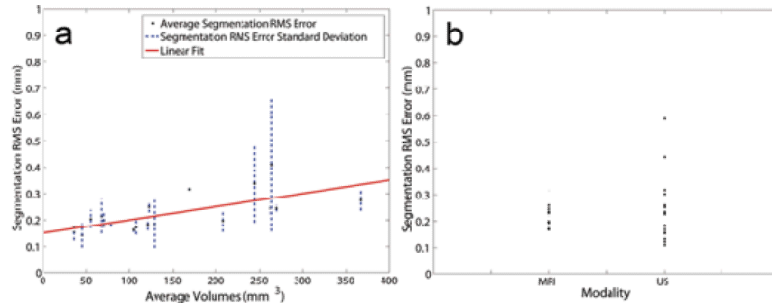
Figure 3.
Registration results for mouse 4 and 7 at time points 1 (A,B; E,F) and 2 (C,D; G,H). Contour lines and cross hairs are drawn, as in Figure 2, to demonstrate registration results. In each of these panels, the arrow and the letters T and M represent the skin layer, center of the tumor, and surrounding muscle, respectively.
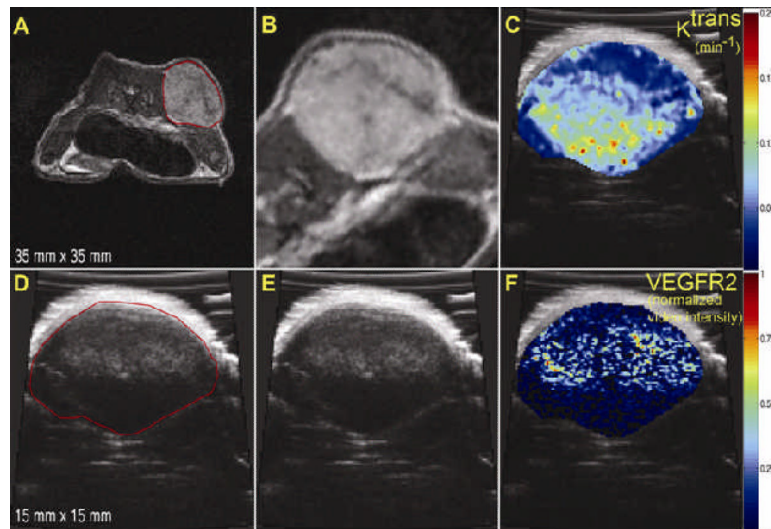
Figure 4.
Results from US-MRI Registration. Panel A: In order to reduce inter-observer variation, boundaries were assessed and volumes for each image set for each modality. The `·' shows the average volume calculated from both investigators and both modalities while the dashed lines (horizontal is MRI and vertical is US) show the error associated with the volume for the respective modality. The data points fit the line of unity with an $r = 0.9997$ ($y = 0.9808x + 1.8441$). Panel B: Average registration RMS error (·) and the associated standard deviations (dashed lines) are plotted versus average volume. The linear fit (solid line) shows an upward trend with increasing volume ($y = 0.0007x + 0.2546$, $r = 0.657$).
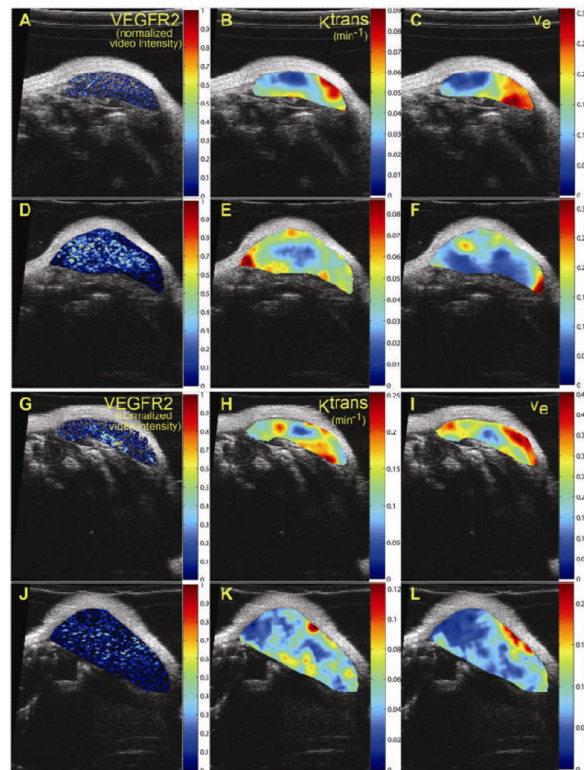
Figure 5.
Results from US-MRI Segmentation. Panel A: Average segmentation RMS error (·) and the associated standard deviations (dashed lines) are plotted versus average volume. The linear fit (solid line) shows a similar increasing trend with increasing volume ($y = 0.0005x + 0.1499$, $r = 0.680$). Panel B: RMS segmentation error is plotted for each modality, depicting a larger variability with segmentation in US than MRI.

Figure 6.
Step by step demonstration of the registration between parametric maps produced by MRI and US. Panels a and d illustrate the segmentation of the tumor from both MRI (A) and US (D). Once the image sets have been registered (panels B and E), transformations are applied to the maps of K^{trans} and VEGFR2 from the respective modalities. The maps can then be compared on a voxel by voxel basis (panels C and F).

Figure 7.
Parametric maps of VEGFR2 distribution, K^{trans}, and v_e for two mice at two time points. Panels A and D and panels G and J show the VEGFR2 distributions for mouse 1 and mouse 4, respectively at both time point while B, E, H, K demonstrate the K^{trans} maps. v_e maps are presented in panels C, F, I, and L. While a spatial correlation between VEGFR2 and v_e maps was not expected, correlation between VEGFR2 and K^{trans} was anticipated; however, both visual and quantitative analysis show that there does not appear to be any significant correlation between these two metrics.

Table 1

RMS registration error recorded for each investigator at each time point.

| Mouse | TimePoint | | | |
| | 1 | | 2 | |
	Investigator 1 RMS Error (mm)	Investigator 2 RMS Error (mm)	Investigator 1 RMS Error (mm)	Investigator 2 RMS Error (mm)
1	0.34	0.41	0.45	0.54
2	0.35	0.26	0.27	0.25
3	0.35	0.24	0.62	0.67
4	0.27	0.32	0.34	0.44
5	0.33	0.26	0.37	0.49
6	0.24	0.27	0.37	0.54
7	0.37	0.39	0.27	0.32
8	0.39	0.37	0.43	0.17
9	0.32	0.31	0.25	0.36
Average	0.33	0.32	0.37	0.42

Table 2

Segmentation comparison between investigators at each time point.

| | TimePoint | | | |
| | 1 | | 2 | |
Mouse	MRI Segmentation RMS Error (mm)	US Segmentation RMS Error (mm)	MRI Segmentation RMS Error (mm)	US Segmentation RMS Error (mm)
1	0.22	0.18	0.25	0.30
2	0.18	0.23	0.17	0.16
3	0.32	0.32	0.24	0.25
4	0.26	0.23	0.23	0.59
5	0.25	0.12	0.26	0.23
6	0.18	0.18	0.23	0.44
7	0.17	0.13	0.19	0.15
8	0.17	0.11	0.20	0.17
9	0.17	0.26	0.17	0.23
Average	0.21	0.20	0.21	0.28